Physics Letters A 483 (2023) 129046

Contents lists available at ScienceDirect

Physics Letters A

journal homepage: www.elsevier.com/locate/pla

Combined effects of thermodynamic factors and external fields for nonlinear optical processes of deformed Mathieu quantum dot containing central impurity

Mustafa Kemal Bahar *, Pınar Başer

Department of Physics, Faculty of Science, Sivas Cumhuriyet University, 58140, Sivas, Turkey

ARTICLE INFO

Article history:
Received 20 June 2023
Received in revised form 19 July 2023
Accepted 25 July 2023
Available online 5 August 2023
Communicated by S. Khonina

Keywords:
Quantum dot
Nonlinear optical properties
Hydrogenic impurity
Screw dislocation

ABSTRACT

The theoretical impact of external parameters such as the hydrostatic pressure, temperature, electric field, magnetic field, as well as the Indium (*In*) concentration and quantum dot width on the nonlinear optical properties of a Mathieu quantum dot (MQD) with a screw dislocation and a hydrogenic impurity at its center, formed by an $In_xGa_{1-x}As/GaAs$ heterojunction, is presented. The wave equation of the system is solved in cylindrical coordinates using the effective mass approximation and the Runge-Kutta-Fehlberg (RKF) method, taking into account the direction of the screw dislocation and the symmetry of the structure. In addition to the screw dislocation, thermodynamic effects, electric and magnetic fields, In concentration, and the width of the MQD have significant effects on the electronic energy levels, dipole matrix elements, and transition frequencies, resulting in important consequences for the nonlinear optical properties. The effects and alternatives of the relevant parameters on the nonlinear optical properties of the MQD with a screw dislocation are discussed in detail. The optical properties that can be altered by these parameters may also be important for experimental studies in determining the optimality of the structure.

1. Introduction

Nanostructures such as zero-dimensional (0D) quantum dots, one-dimensional (1D) quantum wires (QWWs) and nanotubes (NTs), two-dimensional (2D) quantum wells and nanoplates, collectively known as low-dimensional systems, exhibit novel properties in various areas such as optoelectronics, nanophotonics, solar energy conversion, thermoelectric and electrochemical energy storage, chemical and biological sensing [1–7]. Among these nanostructures, quantum dots, which encompass carriers in three dimensions (3D), are semiconductor systems with distinct electronic, optical, and transport properties compared to other low-dimensional nanostructures. Quantum dots, having very small dimensions, exhibit a stronger confinement effect due to their larger bandgap [8]. Due to these significant advantages, quantum dots can emit light in different colors by varying their sizes while using the same material [9]. Due to their adjustable photoluminescent properties through size tuning, quantum dots (QDs) are widely used in optoelectronic devices such as the high-efficiency luminescent devices [10], lasers [11], light-emitting diodes [12], biosensors [13], second harmonic generation in quantum computing [14], and photovoltaic cells [15]. Compared to organic light-emitting diodes (OLEDs), LEDs made from quantum dots have advantages such as longer lifespan, lower power consumption, enhanced color saturation, and lower cost, thanks to the ability to tune emission with narrow emission spectra and a wide range of colors [16]. Hydrogenic impurities in low-dimensional systems play an important role in enhancing the conductivity of semiconductors. Additionally, hydrogenic impurities in quantum dots serve as a useful model to understand the electronic and optical properties of these structures. The electronic and nonlinear optical properties of hydrogenic impurities in low-dimensional structures have been investigated by many researchers [17–20]. In nonlinear optical properties, the relationship between polarization intensity and the electric field of light is known to be non-linear. Nonlinear optical processes include second harmonic generation (SHG) [21], electro-optic effects referred to as Pockels and Kerr effects [21], third harmonic generation (THG) [22], high harmonic generation (HHG) [23], and optical rectification (OR) [24], among others. Furthermore, the nonlinear optical properties are utilized in various areas, such as in the design of fiber optic cables to correct optical aberration defects [25]. In the present study, the nonlinear optical properties of an $In_xGa_{1-x}As/GaAs$ MQD system with a screw dislocation are investigated, taking into account

* Corresponding author.
E-mail addresses: mussiv58@gmail.com (M.K. Bahar), pbaser34@gmail.com (P. Başer).

https://doi.org/10.1016/j.physleta.2023.129046
0375-9601/

variations in the structural parameters under different external influences.

MQDs, which can also be experimentally produced, create a parabolic confinement on electrons. By using $In_xGa_{1-x}As/GaAs$ quantum wells and quantum dots, optoelectronic devices such as edge-emitting lasers, microdisk lasers, and photovoltaic converters with higher performance can be achieved [26]. Furthermore, with recent advancements in crystal growth techniques, mixed-dimensional nanostructures called $In_xGa_{1-x}As/GaAs$ quantum well dots (QWDs) have been obtained, which possess advantageous properties of both quantum wells and quantum dots [27]. Dislocations are regions where atoms are positioned outside the crystal structure. Dislocations arise as a result of applying stress to the structure. The fundamental type of dislocation, known as a screw dislocation, is also a result of shear stress, but the movement of the defect line is perpendicular to both the direction of stress and atomic displacement. Screw dislocations have significant consequences on the electronic and optical properties of materials [28,29]. At the boundary of continuity, a screw dislocation affects a quantum system, such as an isolated magnetic flux tube, leading to the Aharonov-Bohm (AB) interference phenomenon [30,31].

External parameters applied to low-dimensional structures, such as the external electric and magnetic fields, hydrostatic pressure, and temperature, modify the electronic and optical properties by altering the structure's symmetry and effective confinement potential [32]. Since the energy spectra of the structure can be adjusted with these external effects, desired electronic and optical properties can be achieved in device designs by tuning these parameters. Moreover, controlled variations in the effects of external perturbations can regulate the performance of optoelectronic devices. Therefore, these external effects are considered important arguments for investigating the linear and nonlinear optical properties of low-dimensional structures [33–37]. In this regard, the application of hydrostatic pressure to nanostructures increases the effective mass of particles and reduces the dielectric constant and dimension of the system. Due to the changed influence of the applied hydrostatic pressure on the confinement potential, the band structure of the structure can also be modified [38–41]. The application of an electric field and/or hydrostatic pressure on quantum wells has significant effects on the density of states and polarizability of hydrogenic shallow donor impurities [42–44]. The density of impurity states is strongly dependent on hydrostatic stress and electric field, and in the absence of an electric field, the energy level can be degenerate for symmetrical positions of the impurities with respect to the center of the quantum well. Relevant studies demonstrate the importance of properly considering the density of impurity states when electric fields are applied in the structure, as it may be crucial for interpreting future experimental data on optical phenomena related to shallow impurities in quantum well wires. Additionally, the results indicate that having accurate knowledge of the impurity distribution within the structure is essential for a quantitative comparison between theoretical and experimental results concerning the binding energies and optical absorption spectra of donor impurities in multiple quantum well systems under hydrostatic pressure. The linear and nonlinear optical properties and electronic properties of hydrogenic impurities in a spherical quantum dot under an electric field have been investigated [40,45], where the significant impact of the external parameters on both the binding energy and the optical properties of the system is an important result. The nonlinear optical properties of quantum dots under a multi-dimensional confinement potential composed of $Al_{0.3}Ga_{0.7}As/GaAs$ material have been studied using the effective mass approximation [46]. Increase in the potential strength and temperature causes a shift of the absorption resonant peaks to blue, while a decrease in the range of the confinement potential significantly affects the optical absorption characteristics by having the same effect on the quantum dot radius and hydrostatic pressure [46]. The optical absorption and energy spectrum of singly ionized double donor systems in the coupled quantum dot-ring structure have been calculated. The obtained results are remarkable in demonstrating the dependence of electronic and linear-nonlinear optical properties on the size of the quantum dot, hydrostatic pressure, temperature, external parameters such as the electric and magnetic fields, and structural parameters such as aluminum concentration [47]. The effects of *In* segregation, temperature, pressure, external electric field, and structural dimensions on the linear and nonlinear optical properties of lens-shaped quantum dots composed of $In_xGa_{1-x}As/GaAs$ heterostructures have been investigated. The results show that the heterogeneous *In* distribution within the QD causes a redshift, while the *In* segregation in the wetting layer leads to a blueshift. Additionally, the absorption coefficient and refractive index resonant frequencies shift to blue as the strength of the electric field increases due to the increased asymmetry of the structure potential induced by the electric field. In addition, nonlinear optical properties shift to red as temperature increases and to blue as pressure increases [48]. The effects of the structure parameters such as hydrostatic pressure, temperature, QD depth, Al concentration and radius on the second harmonic generation coefficient of the structure that can be adjusted as the quantum dot and quantum ring under the enclosure potential, which is the sum of the quadratic reverse parabolic potential and the modified Gaussian potential obtained from $GaAs/Ga_{1-x}Al_xAs$ semiconductor under the influence of magnetic field, have been investigated [49]. In this study, it was found that increasing hydrostatic pressure, Al concentration, and QD radius shift the SHG resonant frequency to red, while an increase in magnetic field, QD depth, harmonic confinement frequency, and temperature leads to a blueshift of the SHG resonant frequency. Furthermore, it was shown that the SHG resonant amplitudes increase with temperature, Al concentration, QD depth, and radius, but decrease with an increase in magnetic field, hydrostatic pressure, and harmonic confinement frequency [49]. The third harmonic generation (THG) of spherical $GaAs/Ga_{1-x}Al_xAs$ quantum dots with the Deng−Fan−Eckart confinement potential is also an interesting study that explores the dependence on pressure, temperature, and Al concentration [50]. The obtained results reveal that these parameters influence significantly the position and amplitude of the THG coefficient's resonant peak. The peak of the THG coefficient shifts to red with increasing pressure due to the decrease in transition energies with increasing pressure, and the THG resonant amplitudes also increase with increasing pressure. As temperature increases, the THG resonant frequency shifts to blue, albeit with a slight increase in the difference between transition energies. Additionally, contrary to the increase in pressure, the THG amplitudes decrease with increasing temperature [50].

In this study, the nonlinear optical properties (NOR, SHG, and THG) of the hydrogenic impurity in the center of the MQD with screw dislocation have been probed by considering the external effects such as hydrostatic pressure, temperature, external electric field, magnetic field, and the changes in structural parameters. From an application perspective, it is important to determine the optimum conditions by manipulating these external fields and adjusting the structural parameters. Therefore, the main motivation of the study is to explore the effects of the screw dislocation, external electric field, magnetic field, and structural parameters on the NOR, SHG, and THG, aiming to identify the alternatives of these variables to each other. Based on the obtained theoretical results and the determined nonlinear optical properties, it will be possible to create devices or structure components with desired properties more practically and reliably, without requiring extensive experimental experience, to obtain samples with the desired capabilities

in measurements. The results obtained in this study have a manual nature for applications involving MQDs.

The work is organized as follows. Section 2 presents the theoretical calculation procedure. In Section 3, numerical results, electronic properties, and comments on the nonlinear optical coefficients are discussed, and finally, Section 4 presents the obtained results.

2. Theoretical model and procedure

Some type topological defects are depicted by considering the line element

$$ds^2 = g_{ij}dy^i dy^j \tag{1}$$

with g_{ij} (the metric tensor elements), $\{y^i\}$ (the curvilinear coordinate's appropriate set). The Laplacian operator in the relevant curvilinear coordinate system is stated as

$$\nabla^2 = \frac{1}{\sqrt{|\mathbf{g}|}}\partial_i\sqrt{|\mathbf{g}|}g^{ij}\partial_j \tag{2}$$

with $|\mathbf{g}|$ (determinant of the matrix $\mathbf{g} = (g_{ij})$), $\partial_j = \partial/y^i$, $g^{ij}g_{jk} = \delta^i_k$. For such a curvilinear coordinate system, the nonrelativistic wave equation is in the following form (considering natural units);

$$i\frac{\partial\psi}{\partial t} = -\frac{1}{2m}\frac{1}{\sqrt{|\mathbf{g}|}}\partial_i(\sqrt{|\mathbf{g}|}g^{ij}\partial_j)\psi + V(\mathbf{r})\psi, \tag{3}$$

where $V(\mathbf{r})$ is the scalar potential. The metric of the relevant system for the electrons in the $3D$ crystal having the single screw dislocation with the Burgers vector $\mathbf{b} = b\mathbf{e_z}$ along the $z-$axis is given by [51]

$$ds^2 = (dz + \beta d\phi)^2 + dr^2 + r^2 d\phi^2, \tag{4}$$

where ϕ is the azimuthal coordinate, r is the radial coordinate as $r = \sqrt{x^2 + y^2}$, and $(r, \phi, z) \to (r, \phi + 2\pi, z)$, $\beta = b/2\pi$. The Hamiltonian operator for an electron of the effective mass $m^\star$ in a crystal with a screw dislocation includes an effective potential energy function, given by

$$H = -\frac{\hbar^2}{2m^\star}\nabla^2 + V(\mathbf{r}), \tag{5}$$

where the Hamiltonian is obtained by using the continuous limit approach within the framework of the tight-binding model for discrete lattice [52]. This interaction potential contains a potential term resulting from structural distortion having functional impact on the electronic, optical and statistical specifications of the structure in terms of semiconductor's carriers [53]. This additive potential term formed by the screw dislocation can be evaluated as the deformed potential. The deformed potential is stated as the following form

$$V_{SD}(r) = \frac{\hbar^2}{2m^\star a^2}\frac{b^2}{4\pi^2 r^2}(2 + a^2(\frac{\partial}{\partial z})^2), \tag{6}$$

where $m^\star$ is the effective mass of the electron, a is the lattice constant. The Hamiltonian for a hydrogenic impurity at the center of the MQD under the influence of the screw dislocation, the external electric field in the radial direction, the external magnetic field, the hydrostatic pressure, and the temperature is demonstrated by

$$H = \frac{1}{2m^\star(P,T)}\Big[-i\hbar\vec{\nabla} - e\vec{A}\Big]^2 + V_{SD}(r) + V_{MQD}(r) + e\vec{\xi}.\vec{r} - \frac{Ze^2}{4\pi\varepsilon_0\varepsilon(P,T)r}, \tag{7}$$

where $V_{MQD}(r)$ is the MQD potential, $V_{SD}(r)$ is the deformed potential with $m^\star(P,T)$, $\vec{\xi}$ is the external electric field in the radial direction, and the last term is the impurity potential energy. For the encompassed electron in the MQD, the potential energy varies with the radial distance (r). The position of the hydrogenic impurity is central. Since the electron is confined within the quantum dot and also interacts with the central hydrogenic impurity, the added impurity potential energy to the system is considered to vary solely with the radial distance (r). There are various experimental methods for applying a radial electric field to a quantum dot [54]. i) By applying voltage to electrodes specially positioned around the quantum dot, an electric potential difference is created between them, resulting in a radial electric field applied to the quantum dot. ii) In the ionization process, an ion beam with sufficient energy is generated in a region close to the quantum dot. This ion beam creates an electric field that affects the quantum dot and aligns along the desired radial direction. iii) An optical trap can be applied using laser light. The laser light creates a radial electric field by exerting an electromagnetic force on the quantum dot. The effective mass is revised due to the hydrostatic pressure (P) and temperature (T). Then, $m^\star(P,T)$ is given by

$$m^\star(P,T) = \left[1 + E_P^\Gamma\left(\frac{2}{E_g^\Gamma(P,T)} + \frac{1}{E_g^\Gamma(P,T) + 0.341}\right)\right]^{-1} m_0, \tag{8}$$

with the m_0 (the free electron mass). Similarly, the static electric constant is also modified, stating as [55]

$$\varepsilon(P,T) = \begin{cases} 12.74exp(-1.67\times10^{-2}P)exp(9.4\times10^{-5}(T-75.6), \\ \quad \text{if } T \le 200K \\ 13.18exp(-1.73\times10^{-2}P)exp(20.4\times10^{-5}(T-300), \\ \quad \text{if } T > 200K. \end{cases} \tag{9}$$

Considering GaAs (InGaAs), $E_g^\Gamma(P,T)$ including $E_P^\Gamma(P,T) = 7.51$ eV is the energy gap depending on P and T, in units of eV. $E_g^\Gamma(P,T)$ is expressed by

$$E_g^\Gamma(P,T) = E_g^0 + \alpha P - \beta T^2(T + c)^{-1}, \tag{10}$$

with the pressure coefficient $\alpha = 10.8\times10^{-2}$ eV/GPa($\alpha = 7.7\times10^{-2}$ eV/GPa), the temperature coefficients $\beta = 5.405\times10^{-4}$ eV/K ($\beta = 4.19\times10^{-4}$ eV/K) and $c = 204$ K ($c = 271$ K) for GaAs (and InAs). For $P = 0$ GPa and $T = 0$ K, $E_g^0 = 1.52$ eV (0.42 eV) is the energy gap for GaAs (and InAs) [55,56]. $E_g(P,T)$ for $Ga_xIn_{1-x}As$ can be furnished as function P, T and x (In-concentration) in the following form [56].

$$E_g^{GaInAs}(P,T,x) = E_g^{GaAs}(P,T) + \left[E_g^{InAs}(P,T) - E_g^{InAs}(P,T)\right]x - 0.475x(1-x). \tag{11}$$

The quantum dot radius ($R_{dot}(P)$) is fixed depending on the hydrostatic pressure as follows [57,58].

$$R_{dot}(P) = R(0)(1 - 3(S_{11} + 2S_{12})P)^{(1/3)} \tag{12}$$

where

$$C_{11} = (8.34 + 3.56x)10, \tag{13}$$
$$C_{12} = (4.54 + 0.8x)10,$$
$$S_{11} = (C_{11} + C_{12})/((C_{11} - C_{12})(C_{11} + 2C_{12})),$$
$$S_{12} = -C_{12}/((C_{11} - C_{12})(C_{11} + 2C_{12})).$$

The P and T require modification of the MQD profile, and the related modification is expressed by [57,58]

$$V_{MQD}(r,P,T) = \begin{cases} 0.7(E_g^{GaAs}(P,T) - E_g^{GaInAs}(P,T))(sin^2(\eta r) - cos(\eta r)), \\ \quad \text{if } r \le R_{dot}(P) \\ 0, \quad \text{if } r > R_{dot}(P), \end{cases} \tag{14}$$

where η is the width parameter with 1/length- dimension for the MQD.

When considering the uniform external magnetic field ($\vec{B} = B\hat{z}$) along the $z-$axis, being the vector potential $\vec{A}$, the gauge $\vec{\nabla} \times \vec{A} = \vec{B}$ is employed. In this case, if the eigenvalue equation for the Hamiltonian operator in Eq. (7) is ordered, the following differential equation is obtained

$$\begin{aligned} &-\frac{\hbar^2}{2m^\star(P,T)}\left[\frac{\partial^2}{\partial r^2} + \frac{1}{r}\frac{\partial}{\partial r} + \frac{1}{r^2}(\frac{\partial}{\partial \phi} - \beta\frac{\partial}{\partial z})^2 + \frac{\partial^2}{\partial z^2}\right]\Psi(r,\phi,z) \\ &+\left[\frac{ie B\hbar}{2m^\star(P,T)}(\frac{\partial}{\partial \phi} - \beta\frac{\partial}{\partial z}) + \frac{e^2B^2r^2}{8m^\star(P,T)}\right]\Psi(r,\phi,z) \\ &+ (V_{SD}(r,P,T) + V_{MQD}(r,P,T) + e\xi r - \frac{Ze^2}{4\pi\varepsilon_0\varepsilon(P,T)r} \\ &- E)\Psi(r,\phi,z) = 0, \end{aligned} \tag{15}$$

Due to freedom of the electron in the $z-$direction, and its 2π period in the azimuthal direction, the following ansatz for the wave function can be suggested

$$\Psi(r,\phi,z) = NR(r)e^{im_\ell\phi}e^{ik_z z}, \tag{16}$$

where N is the normalization constant, m_ℓ is the magnetic quantum number as $m_\ell = 0, \pm1, \pm2, \pm3, ...$; and $k_z \exists \Re$. Considering the wave function suggestion for the Eq. (15), it is obtained that

$$\begin{aligned} R''(r) + \frac{R'(r)}{r} + \Bigg[&\frac{2m^\star(P,T)E}{\hbar^2} + \frac{eB}{\hbar}(m_\ell - \beta k_z) - k_z^2 - \frac{e^2B^2}{4\hbar^2}r^2 \\ &- \frac{2m^\star(P,T)}{\hbar^2}e\xi r - \frac{(m_\ell - \beta k_z)^2 + \frac{b^2}{4\pi^2a^2}(2 + a^2k_z^2)}{r^2} \\ &+ \frac{2m^\star(P,T)}{\hbar^2}\frac{Ze^2}{4\pi\varepsilon_0\varepsilon(P,T)r} \\ &- \frac{2m^\star(P,T)}{\hbar^2}V_{MQD}(r,P,T)\Bigg]R(r) = 0. \end{aligned} \tag{17}$$

Eq. (17) is solved by employing Runge-Kutta-Fehlberg (RKF) method. For details of the RKF method, please refer [59].

To specify the NOR, SHG and THG characteristics of the MQD system, it is taken into consideration that monochromatic optical radiation field ($E(t)$) having ω frequency is applied in the radial direction, and is given by

$$\mathbf{E}(t) = \tilde{\mathbf{E}}e^{i\omega t} + \tilde{\mathbf{E}}^{-i\omega t}. \tag{18}$$

The time-evolution of the matrix elements of one-electron density operator is stated as [60]

$$\frac{\partial\hat{\rho}_{ij}}{\partial t} = \frac{1}{i\hbar}[\hat{H} - \hat{M}.\mathbf{E}(t), \hat{\rho}]_{ij} - \Gamma_{ij}(\hat{\rho} - \hat{\rho}^{(0)})_{ij}, \tag{19}$$

with $\hat{\rho}$ (density matrix of one-electron system), $\hat{\rho}^{(0)}$ (unperturbed density matrix operator), $\hat{H}_0$ (the Hamiltonian of the system when no electromagnetic field), $\hat{M}.\mathbf{E}(t) = -e\hat{r}E(t)$ (perturbative contribution), Γ_{ij} (the relaxation rate in damping duration). In order to Eq. (10), the following serial solution suggestion can be considered [61]

$$\hat{\rho}(t) = \sum_{n=0}^{\infty}\hat{\rho}^{(n)}, \tag{20}$$

when considering Eq. (20), Eq. (19) is converted to the following form

$$\frac{\partial\hat{\rho}_{ij}^{(n+1)}}{\partial t} = \frac{1}{i\hbar}\left([\hat{H}, \hat{\rho}^{(n+1)}]_{ij} - i\hbar\Gamma_{ij}\hat{\rho}_{ij}^{(n+1)}\right) - \frac{1}{i\hbar}[e\hat{r}, \hat{\rho}^{(n)}]_{ij}E(t). \tag{21}$$

Due to $E(t)$ optical field, the electronic polarization is expressed as [62]

$$\begin{aligned} P(t) = (&\varepsilon_0\chi_\omega^{(1)}\tilde{E}e^{i\omega t} + \varepsilon_0\chi_0^{(2)}\tilde{E}^2 + \varepsilon_0\chi_{2\omega}^{(2)}\tilde{E}^{(2)}e^{2i\omega t} \\ &+ \varepsilon_0\chi_\omega^{(3)}\tilde{E}^{(2)}\tilde{E}e^{i\omega t} + \varepsilon_0\chi_{3\omega}^{(3)}\tilde{E}^{(3)}e^{3i\omega t} + ...), \end{aligned} \tag{22}$$

where ε_0 is the permittivity of free space; $\chi_\omega^{(1)}$, $\chi_0^{(2)}$, $\chi_{2\omega}^{(2)}$, $\chi_\omega^{(3)}$ and $\chi_{3\omega}^{(3)}$ are, respectively, the linear, the optical rectification, the second harmonic generation, the third order and third harmonic generation susceptibilities. By using density-matrix approach and iterative method; NOR, SHG and THG susceptibilities are obtained in the following form [60,63]:

$$\chi_0^{(2)} = \frac{4e^3\rho_\nu}{\varepsilon_0\hbar^2}\mu_{01}^2\delta_{01}\frac{\omega_{10}^2(1 + \Gamma_2/\Gamma_1) + (\omega^2 + \Gamma_2^2)(\Gamma_2/\Gamma_1 - 1)}{[(\omega_{10} - \omega)^2 + \Gamma_2^2][(\omega_{10} + \omega)^2 + \Gamma_2^2]}, \tag{23}$$

$$\chi_{2\omega}^{(2)} = \frac{e^3\rho_\nu}{\varepsilon_0\hbar^2}\frac{\mu_{01}\mu_{12}\mu_{20}}{(\omega - \omega_{10} - i\Gamma_3)(2\omega - \omega_{20} - i\Gamma_3)}, \tag{24}$$

$$\chi_{3\omega}^{(3)} = \frac{e^4\rho_\nu\mu_{01}\mu_{12}\mu_{23}\mu_{30}}{\varepsilon_0\hbar^3(\omega - \omega_{10} - i\Gamma_3)(2\omega - \omega_{20} - i\Gamma_3)}\frac{1}{(3\omega - \omega_{30} - i\Gamma_3)}, \tag{25}$$

where e is the positive electron charge, ρ_ν is the electron density, $\omega_{ij} = (E_i - E_j)/\hbar$ is the transition frequency, $\Gamma_k = 1/T_k$ ($k = 1, 2, 3$) is the damping term related to lifetime of electrons in transition process. $\delta_{01} = |\mu_{00} - \mu_{11}|$ and being ψ_i initial state wave function and ψ_j final state one, $\mu_{ij} = |<\psi_j|r|\psi_i>|$ ($i, j = 0, 1, 2, 3$) is the off-diagonal matrix elements. In consideration of the SHG, THG and NOR characteristic, the numerical setup is considered as $m^* = 0.067m_0$ (m_0 is free electron mass), $\rho_\nu = 3 \times 10^{23}$ m^{-3}, $\varepsilon_{GaAs} = 13.18$, $\varepsilon_0 = 8.854 \times 10^{-12}$ C^2/Nm^2, $\Gamma_{1,2,3} = 1.0$ Thz. The quantum dot radius is taken as $R_{dot} = 6a_0$ throughout the study. The effective Bohr radius is computed as $a_0 = 103.7$ Å [64–66].

3. Result and discussions

In the present work, the effects of the external electric field (ξ) and magnetic field (B), as well as structural parameters such as the dislocation factor (b), potential height (V_0), and quantum dot width (η), on the nonlinear optical properties (NOR, SHG, and THG) of $In_xGa_{1-x}As/GaAs$ MQDs have been examined. The corresponding effective potential is shown in Fig. 1a as a function of radial distance (r) depending on the hydrostatic pressure and in Fig. 1b depending on the temperature. The variations of wave functions for the effective potential and the first four electronic energy levels are shown in Fig. 2a for the electric field, Fig. 2b for the magnetic field, Fig. 2c for the Burgers vector amplitude, Fig. 2d for the potential height, and Fig. 2e for the MQD width, as functions of radial distance.

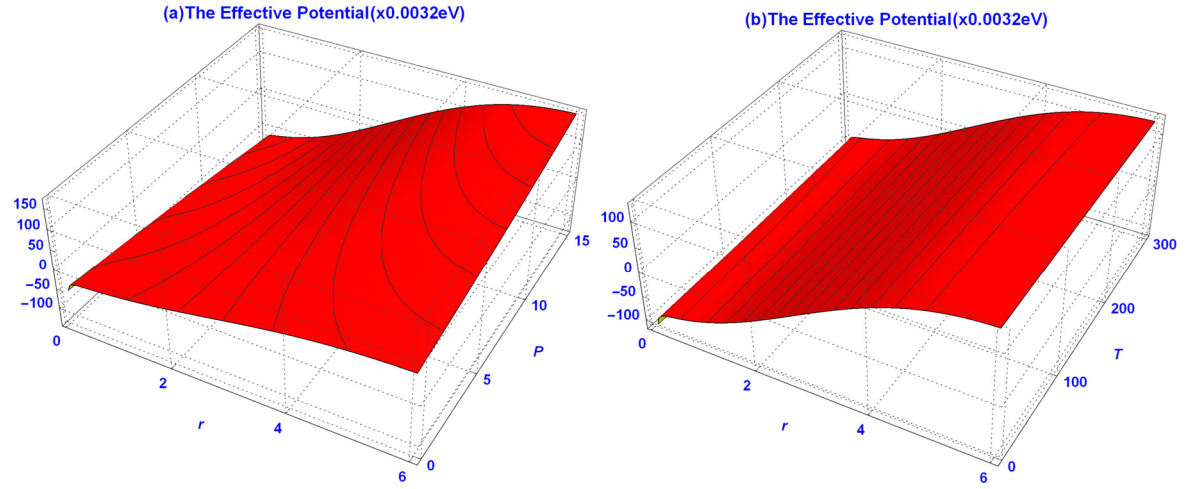

Fig. 1. The effective potential profile as function of the radial distance $r(a_0)$ and, (**a**) the hydrostatic pressure (P (GPa)), when $F = 10$ kV/cm, $B = 0.5$ T, $x = 0.2$, $\eta = 0.35/a_0$, $b = 2a$, $T = 300$ K, (**b**) the temperature ($T(K)$), when $F = 10$ kV/cm, $B = 0.5$ T, $x = 0.2$, $\eta = 0.35/a_0$, $b = 2a$, $P = 10$ GPa.

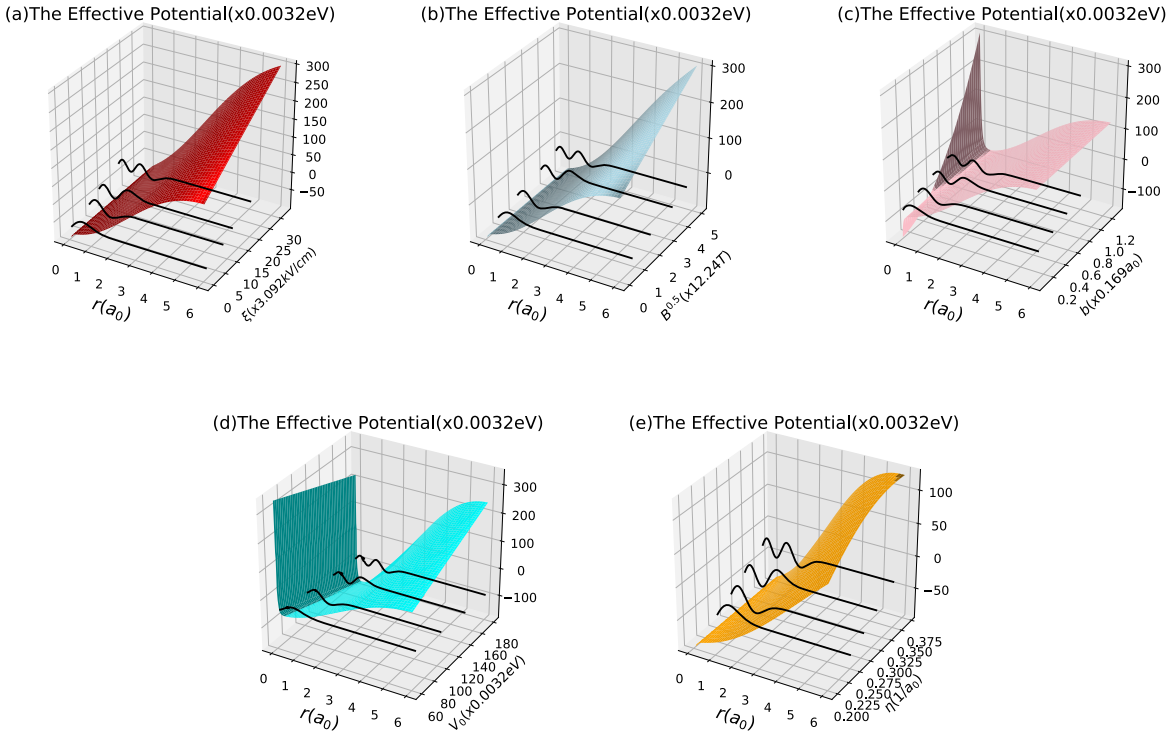

Fig. 2. The effective potential profile and first four bound state wave functions as function of the radial distance $r(a_0)$ and, (**a**) the external electric field (ξ (kV/cm)), when $B = 0.5$ T, $x = 0.2$, $\eta = 0.35/a_0$, $b = 2a$, $P = 10$ GPa, $T = 300$ K, (**b**) the external magnetic field (B (T)), when $\xi = 10$ kV/cm, $x = 0.2$, $\eta = 0.35/a_0$, $b = 2a$, $P = 10$ GPa, $T = 300$ K, (**c**) the Burgers vector magnitude ($b(\times a)$), when $\xi = 10$ kV/cm, $B = 0.5$ T, $x = 0.2$, $\eta = 0.35/a_0$, $P = 10$ GPa, $T = 300$ K, (**d**) the MQD depth (V_0 (eV)), when $\xi = 10$ kV/cm, $\eta = 0.35/a_0$, $b = 2a$, $P = 10$ GPa, $T = 300$ K, (**e**) the MQD width parameter ($\eta(1/a_0)$), when $\xi = 10$ kV/cm, $x = 0.2$, $b = 2a$, $P = 10$ GPa, $T = 300$ K.

In Fig. 3a, b, and c, respectively, the NOR, SHG, and THG of the MQD are shown as functions of the incident photon energy for different hydrostatic pressure values as $P = 1.5$, 5, 10, and 15 GPa. It can be observed that the pressure has a significant effect on all three nonlinear properties. In the NOR, SHG, and THG plots, as the pressure increases, the resonant frequencies shift to red. In Fig. 1a, it can be seen that as the hydrostatic pressure increases, the confinement effect of the structure decreases, especially for large radius values, which leads to a decrease in energy differences (see Figs. 3 insets). Additionally, it is observed that the amplitudes of NOR, SHG, and THG amplitude decrease with increasing pressure. This decrease is consistent with the decrease in matrix elements with pressure for all three plots (see Figs. 3 insets). In Fig. 3b, as the pressure decreases, a second resonant peak starts to appear, in line with the SHG behavior. However, with increasing pressure, a stable and sharp character emerges in the SHG curve, which can be interpreted as the enhancement of frequency doubling possibility due to the increase in hydrostatic pressure. In Fig. 3c, it can be observed that the applied hydrostatic pressure does not change the THG character in terms of resonant frequencies. More clearly, as the hydrostatic pressure increases, two resonant peaks always form.

In Fig. 4a, b, and c, respectively, the NOR, SHG, and THG of the MQD are shown as functions of the incident photon energy for temperature values as $T = 0$, 150, and 300 K. In all three plots, it can be observed that the resonant frequencies shift towards higher

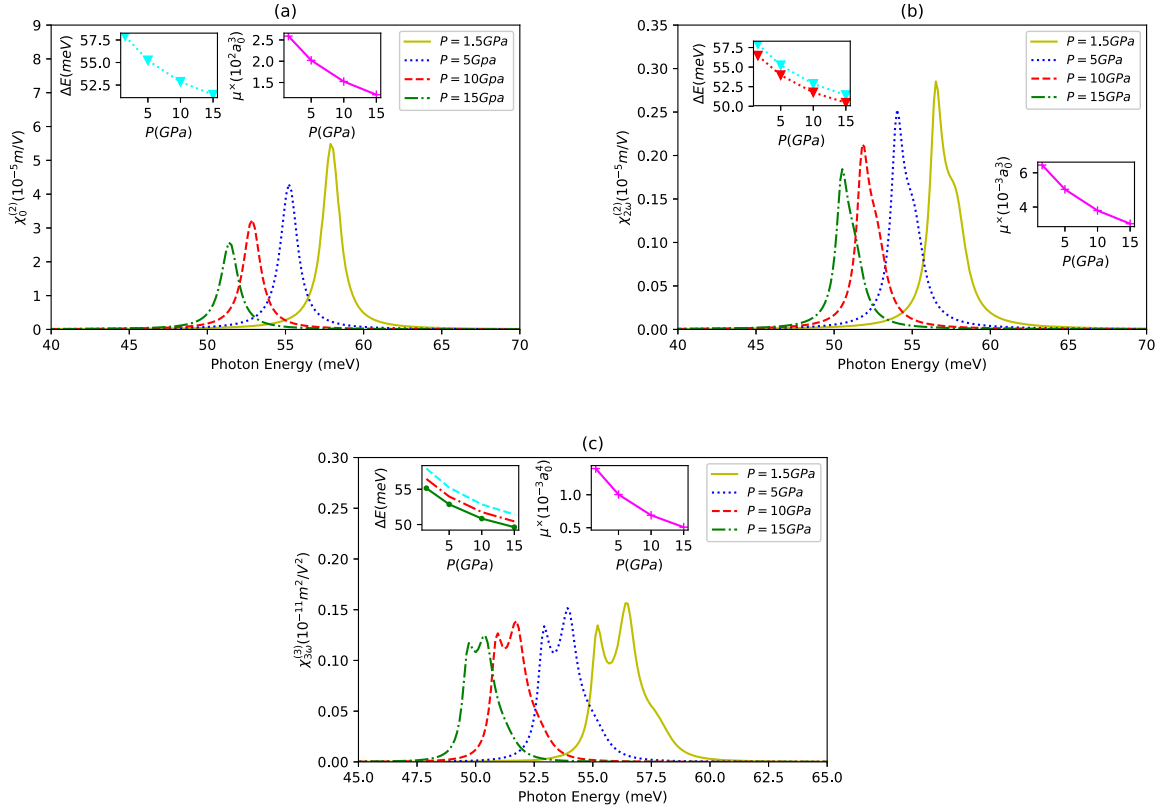

Fig. 3. The NOR (panel **a**), SHG (panel **b**) and THG coefficients (panel **c**) of the MQD with $\xi = 10$ kV/cm, $B = 0.5$ T, $x = 0.2$, $\eta = 0.35/a_0$, $b = 2a$, $P = 1.5 - 5 - 10 - 15$ GPa, $T = 300$ K. The insets present the related energy differences and matrix elements, respectively; as $\Delta E = E_1 - E_0$ (cyan) and $\mu^{\times} = \mu_{01}^2 \delta_{01}$ for the NOR coefficients (panel **a**), $\Delta E = (E_2 - E_0)/2$ (red) and $\mu^{\times} = \mu_{01}\mu_{12}\mu_{20}$ for the SHG coefficients (panel **b**), $\Delta E = (E_3 - E_0)/3$ (green) and $\mu^{\times} = \mu_{01}\mu_{12}\mu_{23}\mu_{30}$ for the THG coefficients (panel **c**).

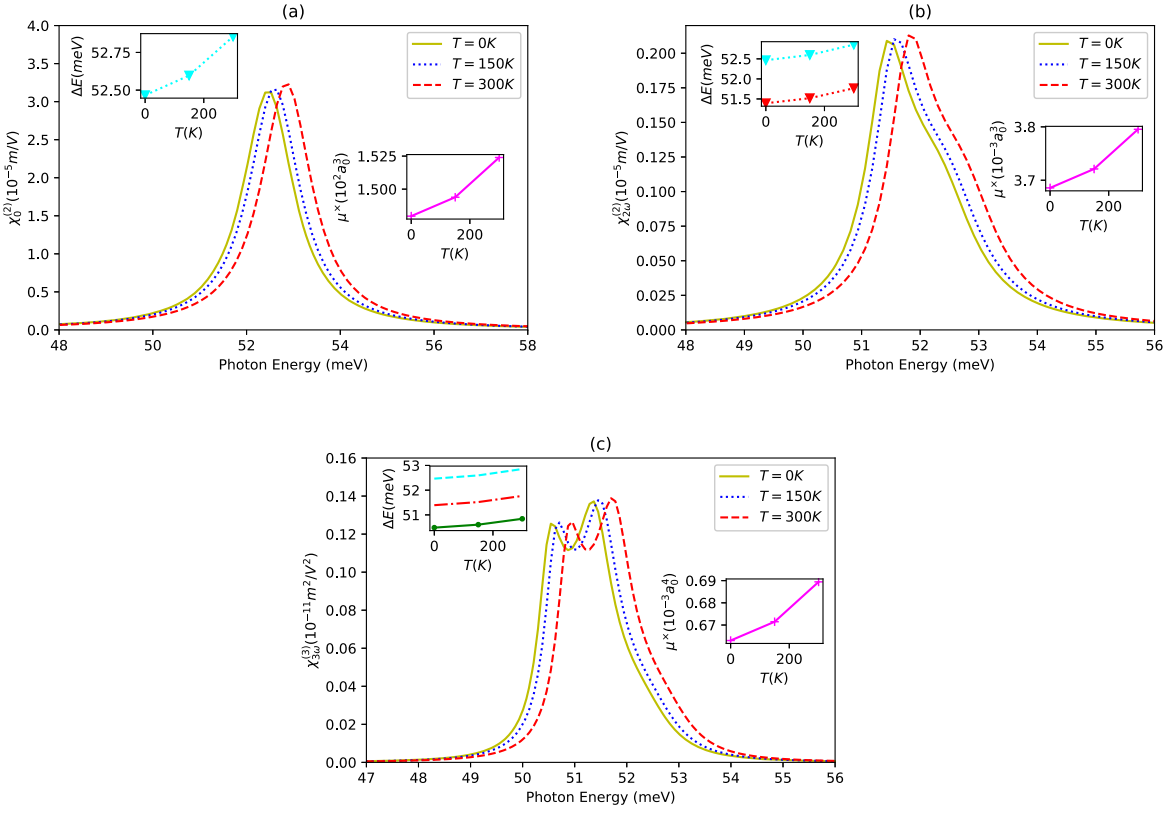

Fig. 4. The same of Fig. 3 but when $T = 0 - 150 - 300$ K.

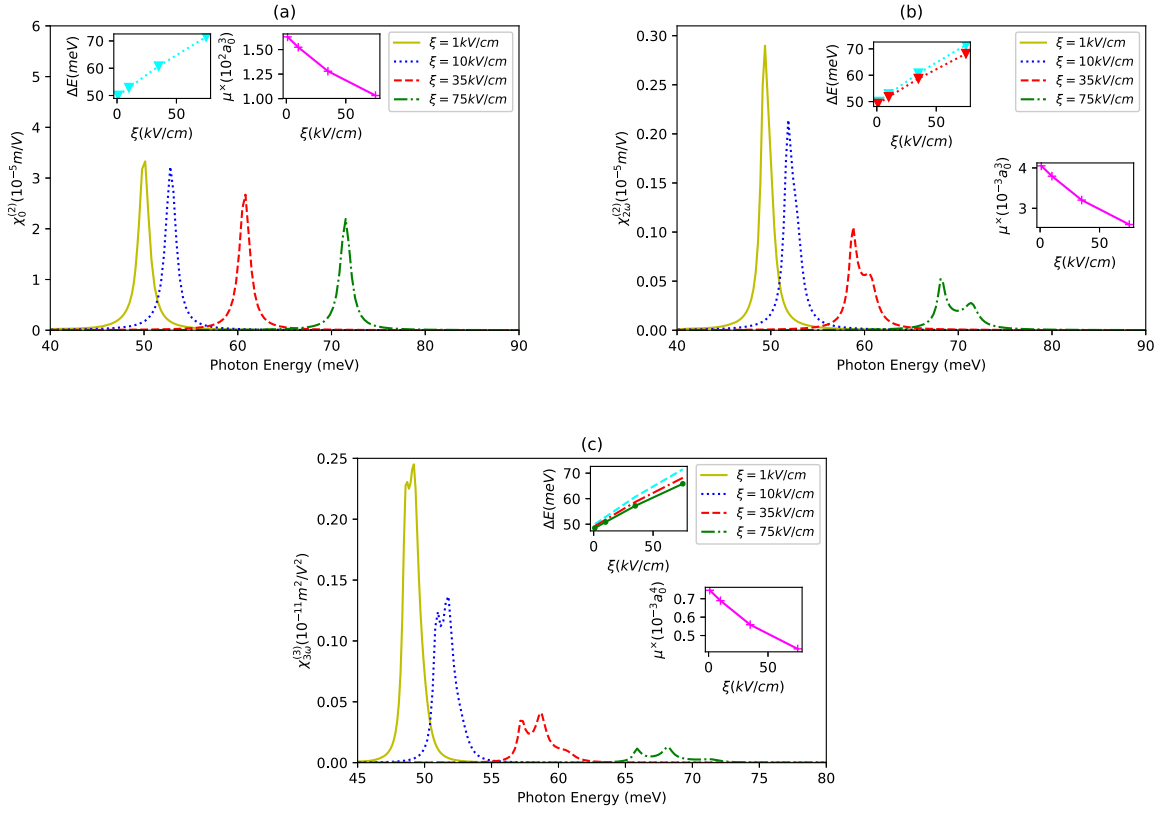

Fig. 5. The NOR (panel **a**), SHG (panel **b**) and THG coefficients (panel **c**) of the MQD with $\xi = 1 - 10 - 35 - 75$ kV/cm, $B = 0.5$ T, $x = 0.2$, $\eta = 0.35/a_0$, $b = 2a$, $P = 10$ GPa, $T = 300$ K. The insets present the related energy differences and matrix elements, respectively; as $\Delta E = E_1 - E_0$ (cyan) and $\mu^{\times} = \mu_{01}^2 \delta_{01}$ for the NOR coefficients (panel **a**), $\Delta E = (E_2 - E_0)/2$ (red) and $\mu^{\times} = \mu_{01}\mu_{12}\mu_{20}$ for the SHG coefficients (panel **b**), $\Delta E = (E_3 - E_0)/3$ (green) and $\mu^{\times} = \mu_{01}\mu_{12}\mu_{23}\mu_{30}$ for the THG coefficients (panel **c**).

energies with increasing the temperature. This can be explained by the temperature effect on the potential energy shown in Fig. 1b. Since the temperature increase generates a weak response on the effective potential, as can be seen from the inset graphs, the energy differences also increase feebly. The weak effect of temperature on the system is the reason for this small difference. A similar weak effect is reflected in the resonant amplitudes, as the NOR, SHG, and THG amplitudes show a weak increase with increasing temperature. The reason for this behavior is the monotonic increase in dipole matrix elements with increasing temperature.

In Fig. 5a, b, and c, respectively, the NOR, SHG, and THG of the MQD are presented as functions of the incident photon energy for different electric field values as $\xi = 1$, 10, 35, and 75 kV/cm. As can be seen in all three plots, as the applied external electric field increases, causing an increase in the energy difference between levels, the NOR, SHG, and THG resonant frequencies shift to blue. As shown in Fig. 2a, as the electric field increases, the symmetry of the structure is disturbed, and the repulsive character of the effective potential becomes dominant, leading to an increase in the energy differences (ΔE) between levels (see Figs. 5 insets). Another noteworthy point in the NOR, SHG, and THG graphs is the decrease in the amplitudes as the electric field increases. In the insets of Fig. 5a, b, and c, it can be observed that as the electric field increases, $\mu^{\times}$ decreases. Therefore, it can be said that the change in dipole matrix elements ($\mu^{\times}$) with respect to the electric field dominates the amplitudes. As the electric field disrupts the symmetry of the MQD (Fig. 2a), it leads to more pronounced SHG effects. In the SHG graph, the first notable point is the transformation of two sharp resonant peaks into a single sharp peak as the electric field decreases. A similar case is observed for THG as well. As the applied electric field strength decreases, the THG curve becomes more stable.

In Fig. 6a, b, and c, respectively, the NOR, SHG, and THG of the MQD are plotted as functions of the incident photon energy for different external magnetic field values as $B = 0.5$, 5, 10, and 20 T. As shown in Fig. 6a, b, and c, as the magnetic field increases, the NOR, SHG, and THG resonant frequencies shift to blue. This is due to the increase in the repulsive nature of the effective potential and the decrease in its strength as a result of the increase in the magnetic field (see Fig. 2b). It is an expected result that such a repulsive potential character increases the energy difference between levels (see Fig. 6a, b, c insets). Another observation in the NOR and SHG graphs is the monotonic decrease in resonant amplitudes as the magnetic field increases. This decrease in amplitudes is consistent with the decrease in matrix elements ($\mu^{\times}$) in response to the increasing magnetic field, as can be seen in Fig. 6a, b insets. It should be noted that the increase in the magnetic field does not affect the SHG character, as a sharp and stable SHG curve is observed in all cases (see Fig. 6b). As shown in Fig. 6c inset, although the matrix elements ($\mu^{\times}$) decrease with increasing magnetic field, this effect does not reflect on the THG amplitudes. Therefore, it can be said that the matrix elements have an effect on THG amplitudes not solely based on their values but also in relation to the resonant frequencies in a different mathematical form. Furthermore, it is also observed that the magnetic field does not dominate on the THG character.

In Fig. 7a, b, and c, respectively, the NOR, SHG, and THG of the MQD are plotted as functions of the incident photon energy for different values of the Burgers vector as $b = 0.5a$, $1.5a$, $2.5a$, and $3.5a$. As shown in Fig. 7a, b, and c, as the screw dislocation defect increases, the NOR, SHG, and THG resonant frequencies shift slightly to red. This is due to the decrease in the confinement effect of the effective potential as the dislocation defect increases, as can be seen in Fig. 2c. This leads to a decrease in the energy

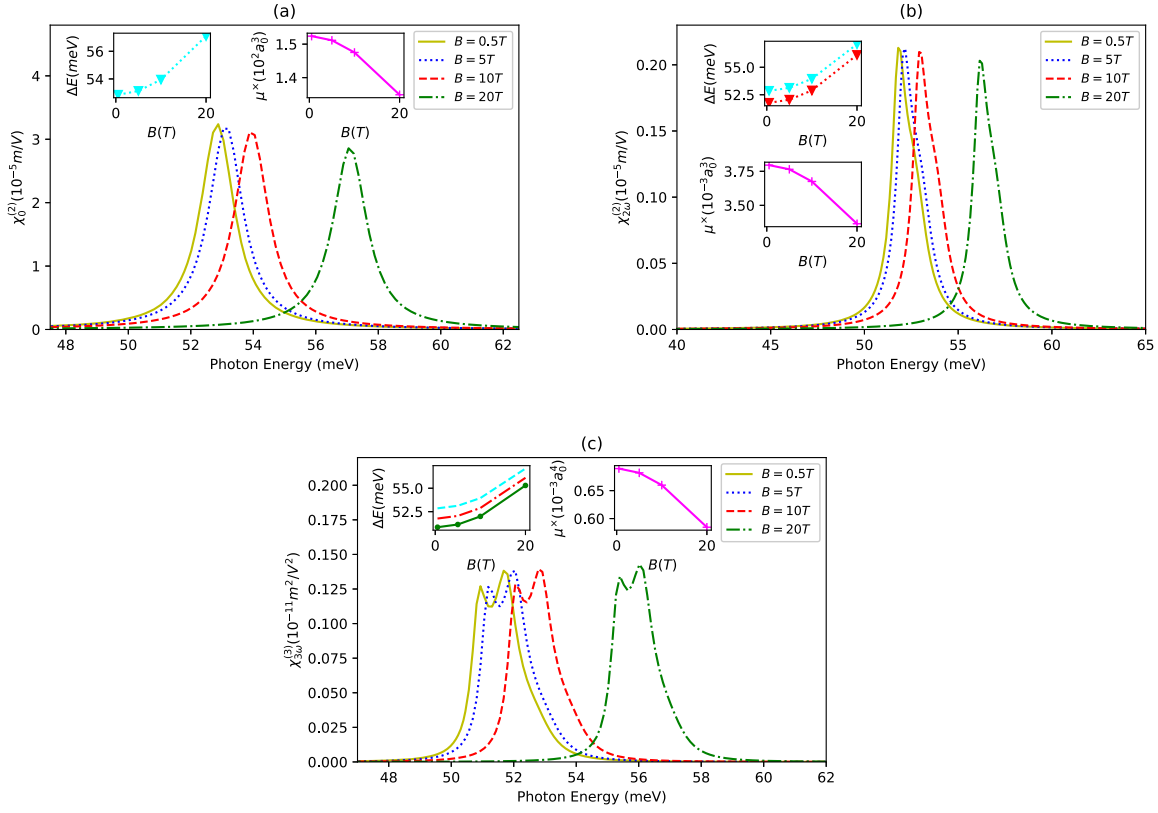

Fig. 6. The same of Fig. 5 but when $\xi = 10$ kV/cm, $B = 0.5 - 5 - 10 - 20$ T, $x = 0.2$, $\eta = 0.35/a_0$, $b = 2a$, $P = 10$ GPa, $T = 300$ K.

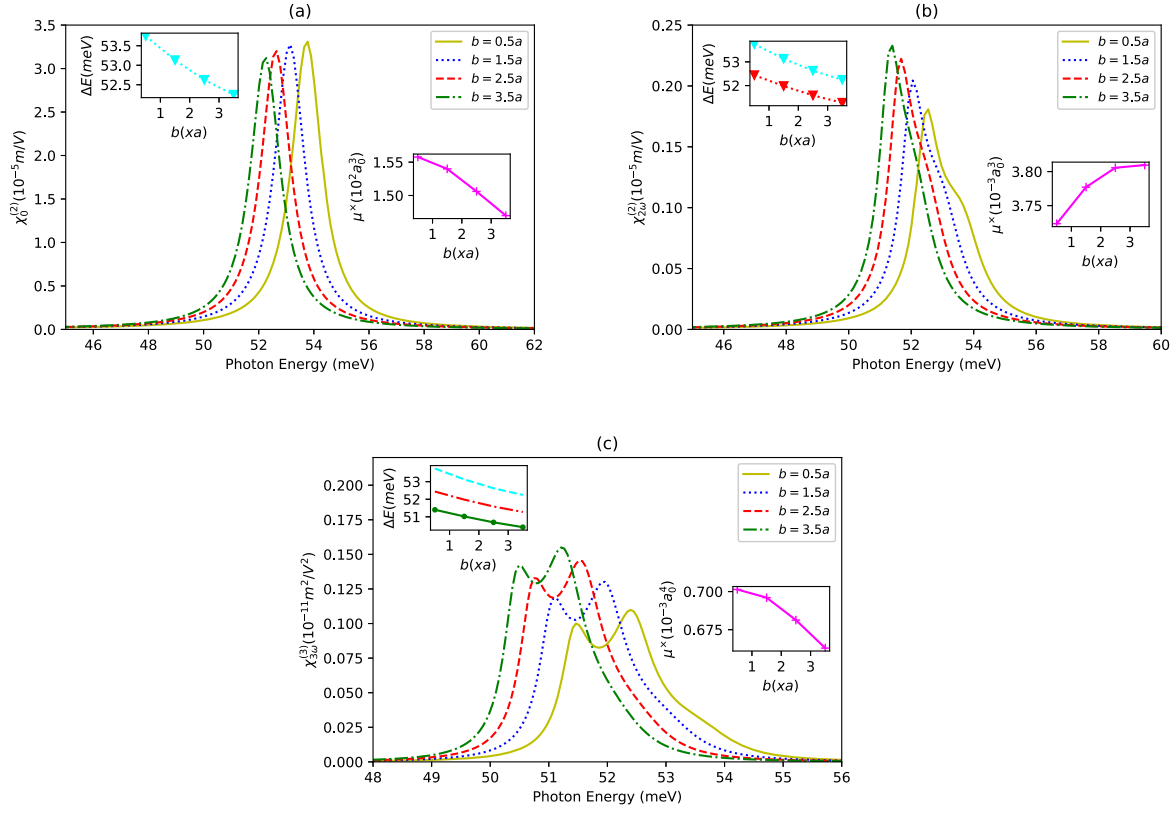

Fig. 7. The same of Fig. 5 but when $\xi = 10$ kV/cm, $B = 0.5$ T, $x = 0.2$, $\eta = 0.35/a_0$, $b = (0.5 - 1.5 - 2.5 - 3.5)a$, $P = 10$ GPa, $T = 300$ K.

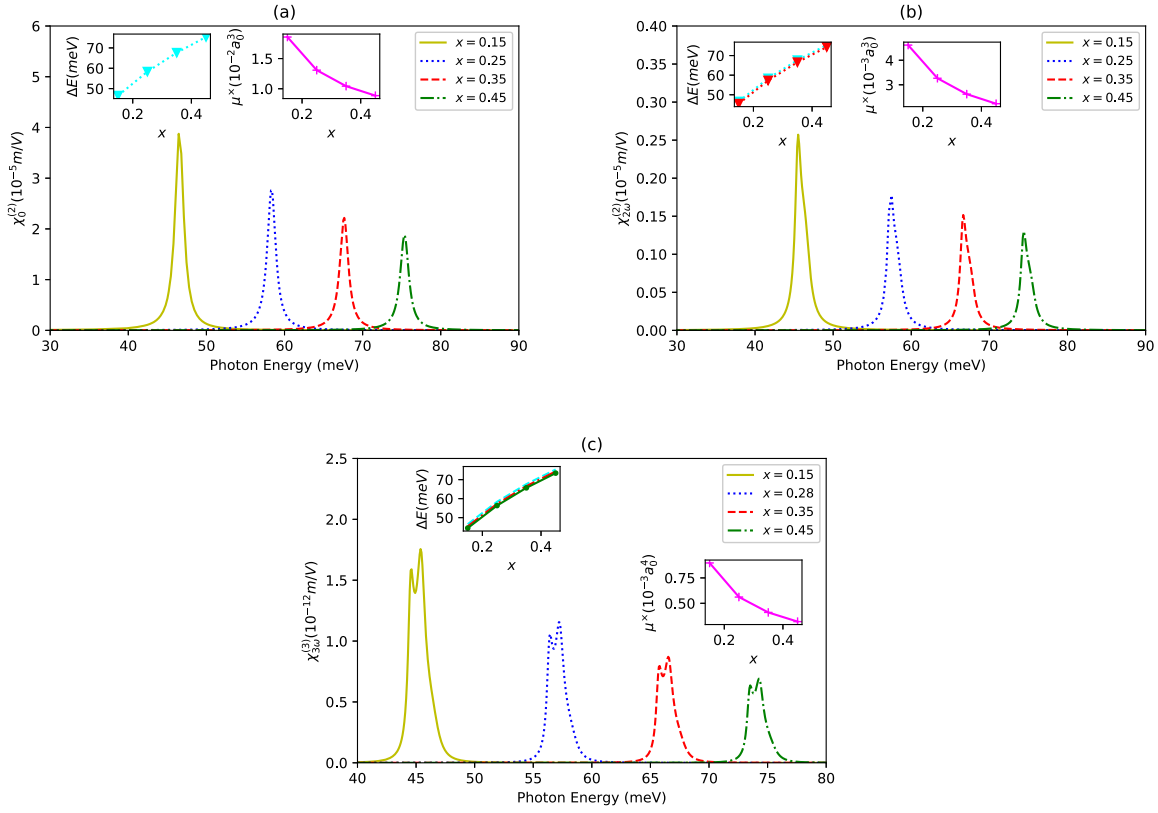

Fig. 8. The same of Fig. 5 but when $\xi = 10$ kV/cm, $B = 0.5$ T, $x = 0.15 - 0.25 - 0.35 - 0.45$, $\eta = 0.35/a_0$, $b = 2)a$, $P = 10$ GPa, $T = 300$ K.

difference between levels. Additionally, although to a lesser extent, the NOR amplitudes decrease slightly as the dislocation defect increases. This decrease in the NOR amplitudes is parallel to the changes in matrix elements caused by the screw dislocation defect. The matrix elements ($\mu^{\times}$) decrease in the same monotonous manner with increasing b value (see Fig. 7a inset). On the other hand, it can be observed that the amplitudes of SHG and THG increase with increasing b, unlike NOR amplitudes. This increase in SHG amplitudes is consistent with the changes in dipole matrix elements, as can be confirmed in Fig. 7. However, there is no parallelism observed in the behavior of dipole matrix elements for the THG amplitudes.

In Fig. 8a, b, and c, respectively, the NOR, SHG, and THG of the MQD are presented as functions of the incident photon energy for different values of *In* concentration as $x = 0.15$, 0.28, 0.35, and 0.45. As x increases, the confinement effect of the effective potential increases, as clearly observed in Fig. 2d, resulting in an increased energy difference between bound state localizations (see Fig. 8a, b, c insets). Consequently, as x increases, the NOR, SHG, and THG resonant energies shift towards the higher energy region. Furthermore, the amplitudes of NOR, SHG, and THG decrease with increasing x, consistent with the changes in matrix elements (see Fig. 8a, b, c insets). In Fig. 9a, b, and c, respectively, the NOR, SHG, and THG of the MQD are presented as functions of the incident photon energy for different values of η as $\eta = 0.25/a_0$, $0.28/a_0$, $0.31/a_0$, and $0.35/a_0$. As seen in Fig. 9a, b, c, as η increases, the NOR, SHG, and THG resonant frequencies shift towards the higher energy region, and the resonant amplitudes decrease. The shift of resonant frequencies towards the higher energy region is consistent with our expectations. As observed in Fig. 2e, as η increases, the repulsive nature of the effective potential increases, thereby increasing the energy difference between localizations (see Fig. 9a, b, c insets). The decrease in resonant amplitudes with increasing η is also consistent with the changes in dipole matrix elements ($\mu^{\times}$) with η.

4. Concluding remarks

In this work, nonlinear optical properties such as the NOR, SHG and THG of $In_xGa_{1-x}As/GaAs$ MQD, which has a hydrogenic impurity in its center, have been probed depending on structural parameters such as In concentration and QD width, as well as external effects such as the electric field, magnetic field, screw dislocation under the effect of hydrostatic pressure and temperature. From a thermodynamic perspective, pressure has a more significant impact on the optical properties. In terms of resonant frequencies, although the external electric and magnetic fields cause similar results, the electric field is found to be more functional when considering optimality. Structural parameters, as expected, have a noticeable effect on the NOR, SHG, and THG. The parameters x and η can be alternative parameters for resonant frequency and amplitude. However, the effect of screw dislocation distinguishes itself in this regard. On the other hand, in this work, the screw dislocation can be regarded as a defect or a mechanical function. The results and analysis presented in this study provide researchers with insights into how to evaluate these parameters in a targeted manner. The parameter values used in the study are consistent with experimental limits and are physically accessible. In this context, we hope that the obtained results and conducted analysis will be beneficial for experimental investigations involving MQD growth.

CRediT authorship contribution statement

Mustafa Kemal Bahar: Writing – review & editing, Visualization, Validation, Supervision, Software, Resources, Project administration, Methodology, Investigation, Funding acquisition, Formal

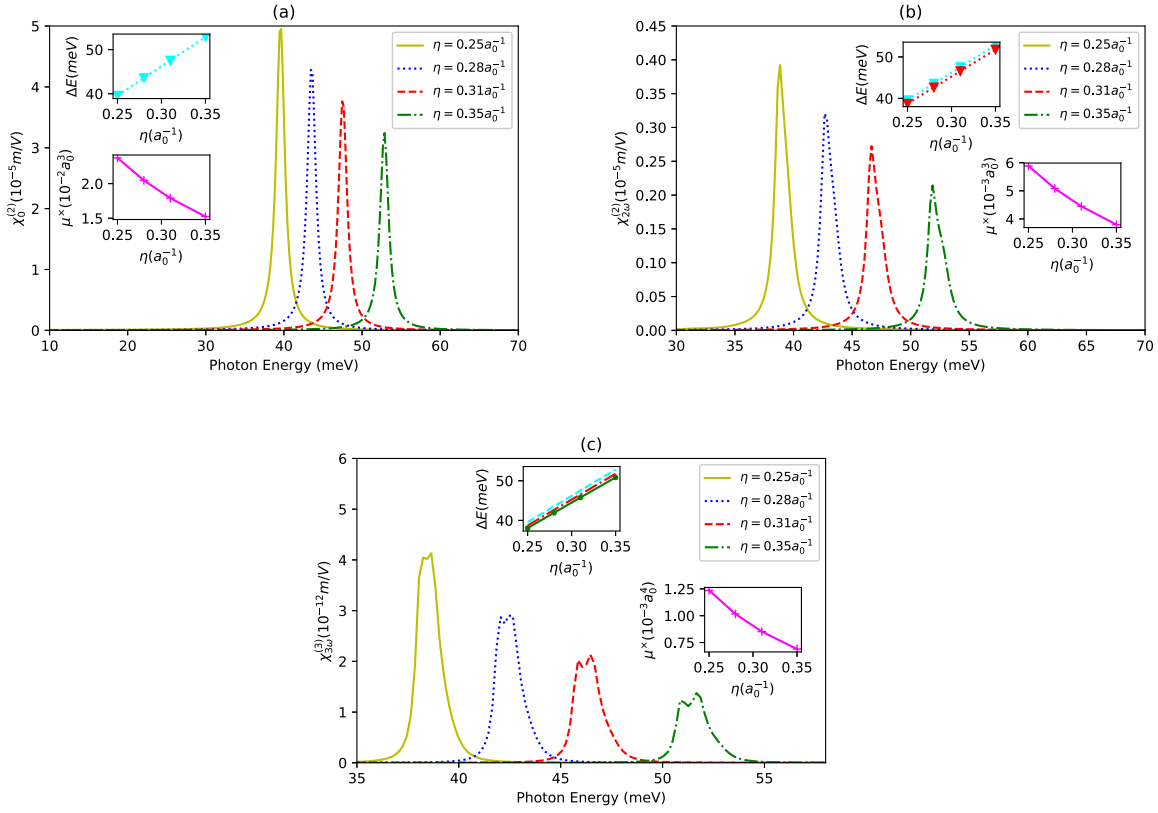

Fig. 9. The same of Fig. 5 but when $\xi = 10$ kV/cm, $B = 0.5$ T, $x = 0.2$, $\eta = (0.25 - 0.28 - 0.31 - 0.35)/a_0$, $b = 2)a$, $P = 10$ GPa, $T = 300$ K.

analysis, Data curation, Conceptualization. **Pınar Başer:** Writing – original draft, Investigation, Data curation.

Declaration of competing interest

The authors declare that they have no known competing financial interests or personal relationships that could have appeared to influence the work reported in this paper.

Data availability

This manuscript has no associated data added to any data repository. The datasets generated during and/or analyzed during the current study are available from the corresponding author on reasonable request.

References

[1] Y. Xia, P. Yang, Y. Sun, Y. Wu, B. Mayers, B. Gates, Y. Yin, F. Kim, H. Yan, One-dimensional nanostructures: synthesis, characterization, and applications, Adv. Mater. 15 (2003) 353.
[2] P. Yang, R. Yan, M. Fardy, Semiconductor nanowire: what's next?, Nano Lett. 10 (2010) 1529.
[3] A.I. Hochbaum, P. Yang, Semiconductor nanowires for energy conversion, Chem. Rev. 110 (2010) 527.
[4] J.R. Szczech, J.M. Higgins, S. Jin, Enhancement of the thermoelectric properties in nanoscale and nanostructured materials, J. Mater. Chem. 21 (2011) 4037.
[5] A.L. Schmitt, J.M. Higgins, J.R. Szczech, S. Jin, Synthesis and applications of metal silicide nanowires, J. Mater. Chem. 20 (2010) 223.
[6] M.J. Bierman, S. Jin, Potential applications of hierarchical branching nanowires in solar energy conversion, Energy Environ. Sci. 2 (2009) 1050.
[7] F. Meng, S.A. Morin, A. Forticaux, S. Jin, Screw dislocation driven growth of nanomaterials, Acc. Chem. Res. 46 (7) (2013) 1616.
[8] A.P. Alivisatos, Perspectives on the physical chemistry of semiconductor nanocrystals, J. Phys. Chem. 100 (1996) 13226.
[9] A.D. Yoffe, Semiconductor quantum dots and related systems: electronic, optical, luminescence and related properties of low dimensional systems, Adv. Phys. 50 (1) (2001) 1.
[10] S.-H. Lee, S.-W. Song, S.-Y. Yoon, D.-Y. Jo, S.-K. Kim, H.-M. Kim, Y. Kim, S.M. Park, H. Yang, Heterostructural tailoring of blue ZnSeTe quantum dots toward high-color purity and high-efficiency electroluminescence, Chem. Eng. J. 429 (2022) 132464.
[11] M.M. Adachi, F. Fan, D.P. Sellan, S. Hoogland, O. Voznyy, A.J. Houtepen, K.D. Parrish, P. Kanjanaboos, J.A. Malen, E.H. Sargent, Microsecond-sustained lasing from colloidal quantum dot solids, Nat. Commun. 6 (2015) 8694.
[12] Y. Shang, Z. Ning, Colloidal quantum-dots surface and device structure engineering for high-performance light-emitting diodes, Nat. Sci. Rev. 4 (2017) 170.
[13] Y. Guo, Q. Cao, C. Zhao, Q. Feng, Stimuli-responsive DNA microcapsules for homogeneous electrochemiluminescence sensing of tumor exosomes, Sens. Actuators B, Chem. 329 (2021) 129136.
[14] H.Y. Ramı ́ez, J. Flo ́rez, A.S. Camacho, Efficient control of Coulomb enhanced second harmonic generation from excitonic transitions in quantum dot ensembles, Phys. Chem. Chem. Phys. 17 (2015) 23938.
[15] G. Yang, W. Liu, Y. Bao, X. Chen, C. Ji, B. Wei, F. Yang, X. Wang, Performance optimization of In (Ga)As quantum dot intermediate band solar cells, Discover Nano 18 (2023) 67.
[16] P. Kathirgamanathan, L.M. Bushby, M. Kumaraverl, S. Ravichandran, S. Surendrakumar, Electroluminescent organic and quantum dot leds: the state of the art, J. Disp. Technol. 11 (2015) 480.
[17] D.S. Chuu, C.M. Hsiao, W.N. Mei, Hydrogenic impurity states in quantum dots and quantum wires, Phys. Rev. B 46 (1992) 3898.
[18] L. Belamkadem, O. Mommadi, M. El Hadi, R. Boussetta, S. Chouef, M. Hbibi, A. El Moussaouy, J.A. Vinasco, C.M. Duque, C.A. Duque, Size and shape effects on effective mass, electronic and optical properties of V-shaped quantum dot: influence of an off-center donor atom, hydrostatic pressure and temperature, J. Comput. Electron. 22 (2023) 29.
[19] P. Rinku Sharma, Impurity-modulated physical and transport properties in a $In_xGa1–xAs$ double quantum wire, Physica B, Condens. Matter 659 (2023) 414845.
[20] M. Gambhir, P. Kumar, T. Kumar, M. Mohan, Investigation of linear and third-order nonlinear optical properties in a laser-dressed parabolic quantum dot with a hydrogenic donor impurity in the presence of a static electric field, Indian J. Phys. 97 (2023) 2169.
[21] F.L. Pedrotti, L.M. Pedrotti, L.S. Pedrotti, Introduction to Optics, 3rd, vol. 510, ISBN 9780131499331, 2017.
[22] A. Ghanbar, Studying third harmonic generation in spherical quantum dot under inversely quadratic Hellmann potential, Opt. Quantum Electron. 55 (2023) 222.

[23] D.N. Yangaliev, V.P. Krainov, O.I. Tolstikhin, Quantum theory of radiation by nonstationary systems with application to high-order harmonic generation, Phys. Rev. A 101 (2020) 013410.
[24] C. Chang, Nonlinear optical refractive index changes of GaAs/AlGaAs quantum dot under tangent-square potential, Phys. Scr. 98 (2023) 045112.
[25] B. Robert, Nonlinear Optics, 3rd., Academic Press, ISBN 978-0-12-369470-6, 2008.
[26] A.M. Nadtochiy, M.V. Maximov, S.A. Mintairov, N.A. Kalyuzhnyy, V.N. Nevedomskiy, S.S. Rouvimov, A.E. Zhukov, Gradual evolution from quantum-well-like to quantum dot-like characteristics in InGaAs/GaAs nanostructure, Phys. Status Solidi B 255 (2018) 180012.
[27] S.A. Mintairov, N.A. Kalyuzhnyy, M.V. Maximov, A.M. Nadtochiy, S. Rouvimov, A.E. Zhukov, GaAs quantum well-dots solar cells with spectral response extended to 1100 nm, IEEE Electron Device Lett. 51 (2015) 1602.
[28] H. Taira, H. Shima, Optical conductivity of semiconductor crystals with a screw dislocation, Solid State Commun. 177 (2014) 61.
[29] D.C. Look, J.R. Sizelove, Dislocation scattering in GaN, Phys. Rev. Lett. 82 (1999) 1237.
[30] R. Bausch, R. Schmitz, L.A. Turski, Scattering of electrons on screw dislocations, Phys. Rev. B, Condens. Matter Mater. Phys. 59 (1999) 13491.
[31] Y. Aharonov, D. Bohm, Significance of electromagnetic potentials in the quantum theory, Physical Review Open Access 115 (1959) 485.
[32] C. Dane, H. Akbaş, A. Guleroğlu, S. Minez, K. Kasapoğlu, The hydrostatic pressure and electric field effects on the normalized binding energy of hydrogenic impurity in a GaAs/AlAs spherical quantum dot, Physica E, Low-Dimens. Syst. Nanostruct. 44 (2011) 186.
[33] C.A. Duque, N. Porras-Montenegro, Z. Barticevic, M. Pacheco, L.E. Oliveira, Effects of applied magnetic fields and hydrostatic pressure on the optical transitions in self-assembled InAs/GaAs quantum dots, J. Phys. Condens. Matter 18 (2006) 1877.
[34] J. Ganguly, S. Saha, A. Bera, M. Ghosh, Modulating optical rectification, second and third harmonic generation of doped quantum dots: interplay between hydrostatic pressure, temperature and noise, Superlattices Microstruct. 98 (2016) 385.
[35] A. Fakkahi, A. Sali, M. Jaouane, R. Arraou, Hydrostatic pressure, temperature, and electric field effects on the hydrogenic impurity binding energy in a multilayered spherical quantum dot, Appl. Phys. A 127 (2021) 908.
[36] Y. Duan, X. Li, C. Chang, Z. Zhao, L. Zhang, Effects of hydrostatic pressure, temperature and Al-concentration on the second-harmonic generation of tuned quantum dot/ring under a perpendicular magnetic field, Physica B, Condens. Matter 631 (2022) 413644.
[37] F. Ungan, R.L. Restrepo, M.E. Mora-Ramos, A.L. Morales, C.A. Duque, Intersubband optical absorption coefficients and refractive index changes in a graded quantum well under intense laser field: effects of hydrostatic pressure, temperature and electric field, Physica B 434 (2014) 26.
[38] M. Zuhair, Hydrostatic pressure and electric-field effects on the electronic and optical properties of InAs spherical layer quantum dot, Physica E, Low-Dimens. Syst. Nanostruct. 46 (2012) 232.
[39] S. Liang, W. Xie, Effects of the hydrostatic pressure and temperature on optical properties of a hydrogenic impurity in the disc-shaped quantum dot, Physica B, Condens. Matter 406 (2011) 2224.
[40] A. El Moussaouy, N. Ouchani, Y. El Hassouani, D. Abouelaoualim, Temperature and hydrostatic pressure effects on exciton–phonon coupled states in semiconductor quantum dot, Superlattices Microstruct. 73 (2014) 22.
[41] A.M. Elabsy, Effect of temperature on the binding energy of a confined impurity to a spherical semiconductor quantum dot, Phys. Scr. 59 (1999) 328.
[42] A. Montes, C.A. Duque, N. Porras-Montenegro, Density of shallow-donor impurity states in rectangular cross section GaAs quantum-well wires under applied electric field, J. Phys. Condens. Matter 10 (1998) 5351.
[43] A.L. Morales, A. Montes, S.Y. López, N. Raigoza, C.A. Duque, Donor-related density of states and polarizability in a GaAs-(Ga, Al)As quantum-well under hydrostatic pressure and applied electric field, Phys. Status Solidi C 652 (2003) 2.
[44] N. Raigoza, A.L. Morales, C.A. Duque, Effects of hydrostatic pressure on donor states in symmetrical GaAs–$Ga_{0.7}Al_{0.3}As$ double quantum wells, Physica B 363 (2005) 262.
[45] M. Kırak, Y. Altınok, S. Yılmaz, The effect of the hydrostatic pressure and temperature on binding energy and optical properties of a donor impurity in aspherical quantum dot under external electric field, J. Lumin. 136 (2013) 415.
[46] X. Wang, X. Li, Nonlinear optical properties of $Al_{0.3}Ga_{0.7}As$/GaAs quantum dots under tunable parameters, Basic Solid State Physics (2023).
[47] N. Hernández, R.A. Lopez-Doria, M.R. Fulla, Optical and electronic properties of a singly ionized double donor confined in coupled quantum dot-rings, Physica E, Low-Dimens. Syst. Nanostruct. 151 (2023) 115736.
[48] N. Benzerroug, D. Makhlouf, M. Choubani, Effects of pressure, temperature, and electric field on linear and nonlinear optical properties of $In_xGa_{1-x}As$/GaAs strained quantum dots under In segregation and In/Ga intermixing phenomena, Physica B, Condens. Matter 658 (2023) 414819.
[49] Y. Duan, X. Li, C. Chang, Z. Zhao, L. Zhang, Effects of hydrostatic pressure, temperature and Al-concentration on the second-harmonic generation of tuned quantum dot/ring under a perpendicular magnetic field, Physica B, Condens. Matter 631 (2022) 413644.
[50] X. Li, Y. Duan, Third-harmonic generation in spherical quantum dots under Deng—Fan—Eckart potential: effects of hydrostatic pressure, temperature and Al-concentration, Physica E, Low-Dimens. Syst. Nanostruct. 144 (2022) 115453.
[51] M.O. Katanaev, I.V. Volovich, Theory of defects in solids and three-dimensional gravity, Ann. Phys. 216 (1992) 1.
[52] R. Bausch, R. Schmitz, L.A. Turski, Single-particle quantum states in a crystal with topological defects, Phys. Rev. Lett. 80 (1998) 2257.
[53] R. Bausch, R. Schmitz, U.A. Turski, Quantum motion of electrons in topologically distorted crystals, Ann. Phys. 8 (1999) 181.
[54] K. Umashankar, Introduction to Engineering Electromagnetic Fields, World Scientific, 1989.
[55] S. Chaudhuri, Hydrogenic-impurity ground state in GaAs/$Ga_{1-x}Al_xAs$ multiple—quantum-well structures, Phys. Rev. B 28 (1983) 4480.
[56] GaAs Adachi, S. AlAs, $Al_xGa_{1-x}As$: material parameters for use in research and device applications, J. Appl. Phys. 58 (1985) R1.
[57] S. Paul, J.B. Roy, P.K. Basu, Empirical expressions for the alloy composition and temperature dependence of the band gap and intrinsic carrier density in $Ga_xIn_{1-x}As$, J. Appl. Phys. 69 (1991) 827.
[58] H.M. Baghramyan, M.G. Barseghyan, A.A. Kirakosyan, Effects of hydrostatic pressure and temperature on interband optical transitions in InAs/GaAs vertically coupled double quantum dots, J. Phys. Conf. Ser. 350 (2012) 012017.
[59] K. Kılıç, M.K. Bahar, Optical response of plasma processed quantum dot under the external fields, Int. J. Quant. Chem. 121 (2021) e26564.
[60] Y.B. Yu, H.J. Wang, Third-harmonic generation in two-dimensional pseudo-dot system with an applied magnetic field, Superlattices Microstruct. 50 (2011) 252.
[61] E. Rosencher, Model system for optical nonlinearities: asymmetric quantum wells, Phys. Rev. B 252 (1991) 44.
[62] G. Rezaei, B. Vaseghi, F. Taghizadeh, M.R.K. Vahdani, M.J. Karimi, Intersubband optical absorption coefficient changes and refractive index changes in a two-dimensional quantum pseudodot system, Superlattices Microstruct. 48 (2010) 450.
[63] R.W. Boyd, Nonlinear Optics, third edition, Rochester, New York, 2007.
[64] S. Paul, J.B. Roy, P.K. Basu, Empirical expressions for the alloy composition and temperature dependence of the band gap and intrinsic carrier density in $Ga_x In_{1-x}As$, J. Appl. Phys. 69 (1991) 827.
[65] F. Ungan, M.K. Bahar, M.G. Barseghyan, L.M. Perez, D. Laroze, Effect of intense laser and electric fields on nonlinear optical properties of cylindrical quantum dot with Morse potential, Optik 236 (2021) 16662.
[66] P. Baser, M.K. Bahar, Evaluation of the external electric- and magnetic field-driven Mathieu quantum dot's optical observables, Physica B, Condens. Matter 639 (2022) 413991.